Nano Energy 92 (2022) 106748

Contents lists available at ScienceDirect

Nano Energy

journal homepage: www.elsevier.com/locate/nanoen

Pair directed silver nano-lines by single-particle assembly in nanofibers for non-contact humidity sensors

Jing He, Xiaotong Zheng *, Zhiwen Zheng, Degang Kong, Kai Ding, Ningjun Chen, Haitao Zhang, Weiqing Yang *

School of Materials Science and Engineering, Key Laboratory of Advanced Technologies of Materials, Ministry of Education, Southwest Jiaotong University, Chengdu 610031, China

ARTICLE INFO

Keywords:
Ag nano-lines
Pair directed
Single-nanoparticle assembly
Multi-stage template
Humidity sensors

ABSTRACT

Shape-controlled nano-silvers have great promise for the practical applications in devices due to their unique electronic properties. Although variously complicated nano-silver structures have been reported, the accurate control of one-dimension (1D) oriented assembly of Ag crystals remains challenging. Here, we innovatively fabricated Ag nano-lines (AgNLs) with pair directed arrays along the parallel boundary of the templated nanofibers. The multi-stage template mechanism of polyvinyl pyrrolidone (PVP) molecules based on electrospinning and UV irradiation played an indispensable effect in the coherent single-nanoparticle assembly of Ag nanocrystals in the nanofibers. Using the electrochemically assisted analysis, we found the special electron conduction and sensibility of water molecules in the AgNLs. Further, based on the tightly connected and gapped assembly characteristics of the AgNLs, we integrated the AgNLs arrays as the nanoscale humidity sensors which behaved the different sensing properties at low, middle and high relative humidity (RH). Our research demonstrated the application of AgNLs in the humidity-relative fields and provided a new strategy for fabricating the nanoscale 1D directed non-contact humidity sensors.

1. Introduction

Multifunctional nano-structured silvers such as AgNPs [1–3], AgNWs [4–6], AgNFs [7,8], Ag super clusters [9], Ag nanoplates [10] and Ag-decorated composites [11,12] have shown great potential in the state-of-the-art technology fields, especially in the area of SERS [13,14], flexible electronics [15,16], electromagnetic interference shielding [17,18], energy [19,20] and biomedical engineering [21–23]. Usually, these nano-silvers were synthesized by the chemical method with the strict requirement for the reaction environment, for example, Ag nanocrystals with the tailored shapes were regulated by the high nucleation temperature and the strictly quantitative reducing agent and capping agent [24,25]. However, it was difficult to control the directed growth and arrangement of Ag nanoparticles. Thus, some template-assisted methods could be used to accurately fabricate Ag nanoparticles with the special pattern and alignment [26–28]. Where, the electrospinning technique provided a convenient approach for the fabrication of Ag nanoparticles with the directional characteristics on the nanofibers [29,30].

Although the Ag composite nanofibers have reported the potential in electricity, optics and biology [31,32], there is no precise assembly of the nucleating particles using the physical adsorption during electrospinning process. Up to this point, the directional structure of Ag nanoparticles in nanofibers are only achieved by regulating the accumulated amount and space of the nanoparticles. Then, the electric sensitivity and conductivity of Ag nanoparticles distributed in whole fibers are limited for the application at a smaller scale. Thus, considering the directional growth and assembly of Ag nanoparticles at one-dimensional scale is an important topic.

Herein, we explored a feasible fabrication process for the directional Ag nanocrystals in composite nanofibers, a new nanostructure of AgNLs was built by the single-nanoparticle assembly in the electrospinning and in-situ UV irradiation reduction of PVP nanofibers. From Ag^{+} to Ag^{0}, PVP chains respectively played three roles of the complexed template (Fig. 1a), field-transferred template (Fig. 1b) and molecule-directed template (Fig. 1c) in the solution blend, electrospinning and in-situ reduction process. By combining the inherent reducibility, complexation and photodegradation of PVP [33–35], Ag nanocrystals tended to fuse with adjacent one along the boundary of nanofibers and formed the

* Corresponding authors.
E-mail addresses: zhengxt@swjtu.edu.cn (X. Zheng), wqyang@swjtu.edu.cn (W. Yang).

https://doi.org/10.1016/j.nanoen.2021.106748
Received 14 October 2021; Received in revised form 12 November 2021; Accepted 14 November 2021
Available online 24 November 2021

pair directed AgNLs. Moreover, compared with the multi-dimension architectures of humidity sensors [36], the very low and high hydrated contents could be easily detected because H_2O molecules filling in AgNLs might form the multi-stage conductive paths. According to the designed patterns of the template nanofibers in electrospinning process [37], the pair directed AgNLs have many promising applications such as the nanoscale fiber electronics [38], molecular detection [39] and bioenergy [40].

2. Results and discussion

The fabrication procedure of the AgNLs spontaneously assembled in PVP nanofibers via electrospinning and UV irradiation is shown in Fig. S1. We built the first-stage structure of the composite nanofibers using PVP as the fiber substrate rather than other polymers, because the inherent complexation of PVP could provide the chance of attachment site and field-oriented carrier for Ag ions. The complexed template effect started by preparing a $AgNO_3$/PVP precursor solution, wherein PVP was a great stabilizer and dispersant for the coordination with Ag^+. Fig. 2a shows the molecular structure of Ag^+ evenly dispersed on the coordinate sites of PVP chains as a complexed template. It has been reported that the solvent evaporation rate and the phase separation rate may create the hollow nanofibers during electrospinning. In this work, ethanol and distilled water were used as solvent, while ethanol was also served as the promoter of phase separation for its good volatility.

Subsequently, in the electrospinning code, PVP chains could be the filed-transferred template as shown in Fig. 2b. Ag^+ is subjected to both the solvent evaporation force (F_S) and electric force (F_E). Here, the distribution of F_E is uneven [41], leading the PVP chains to be stretched straightly and Ag^+ enwrapped in PVP molecules to move towards the surface of the composite nanofibers when ethanol evaporates rapidly through the boundary [42]. As a result, Ag^+ distributed in the inside of nanofibers shifts with the PVP chains to the surface of nanofibers under the field-transferred template effect.

As quantitatively analyzed in Ag model system, the concentration and molecular weight of PVP are critical in tuning the morphology for many types of nanoparticles [24]. Two parameters including the ratio of $AgNO_3$/PVP in the precursor solution and UV irradiation time are identified to play the important role in the nucleus growth of Ag nanoparticles and the precursor formation of AgNLs. Here, we carried out the measurement on the concentration of $AgNO_3$ at 1%, 3%, 5% and 8% in the precursor solution, the obvious AgNLs could form only when the concentration of $AgNO_3$ was 5% (Fig. S2).

To demonstrate the formation mechanism of AgNLs, the precursor nanofibers with different UV irradiation time were characterized. As shown in Fig. 2c, the peaks at 3424, 2959 and 1654 cm^{-1} are the typical adsorption peaks of O–H stretching vibration, C–H asymmetric stretching vibration and C=O stretching vibration, respectively. These peaks appear in all samples. It is worth noting that the peaks at 1660 and 1652 cm^{-1} belong to C=O stretching vibration because of the heterogenous molecular weight of PVP (Fig. 2d). The peak at 1656 cm^{-1} slightly shifting to lower value in electrospun precursor nanofibers, is probably due to the interaction between PVP and Ag ions. Furthermore, the same peak in AgNLs/PVP composite after UV irradiation further shifts to 1649 cm^{-1}, which proves that more Ag nanoparticles have emerged (Fig. S3). Fig. 2e shows that the Raman shifts at about 1357 and

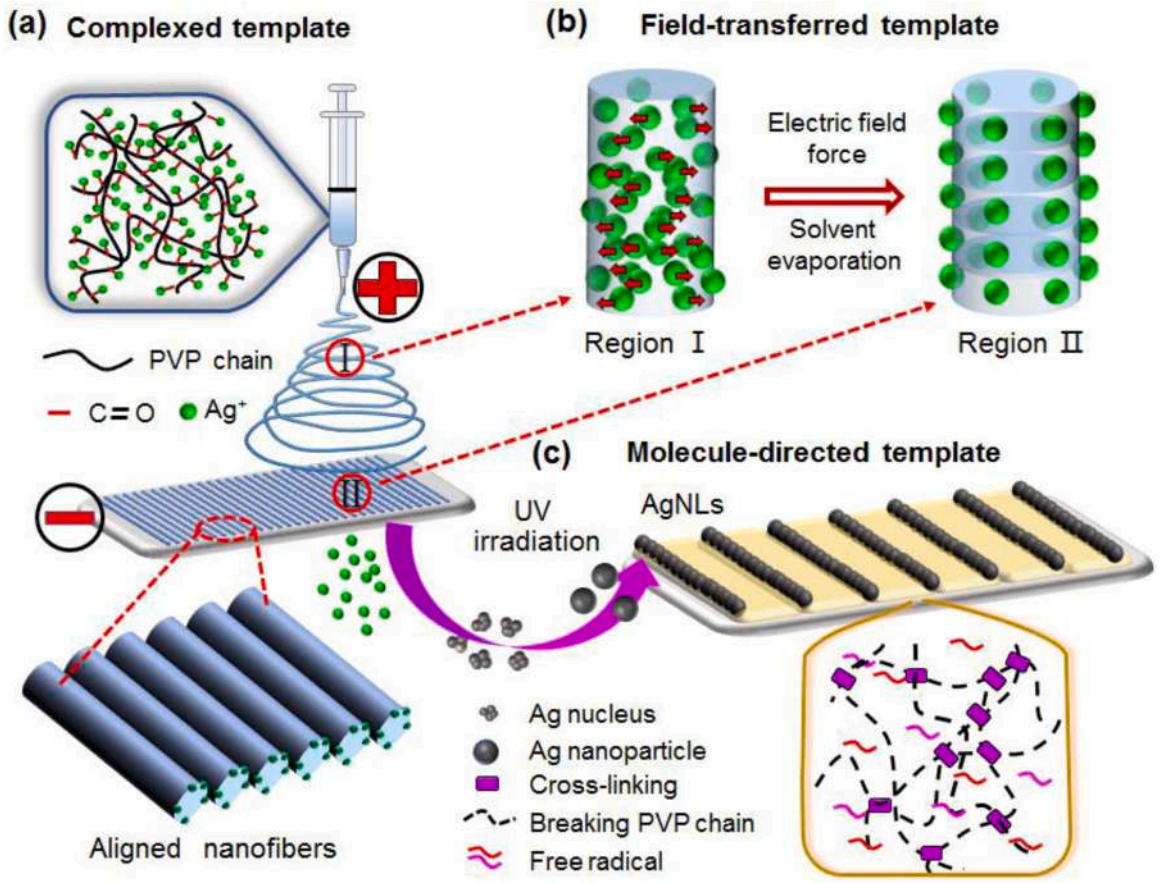

Fig. 1. Schematic diagram of the pair directed AgNLs by single-particle assembly in the composite nanofibers. (a), The complexed template effect of PVP chains on Ag^+ uniformly dispersed in the precursor solution. (b), The distribution of Ag^+ from the inside of the composite nanofibers to the surface by the electric field force and solvent evaporate force in the electrospinning. (c), The aligned assembly of the Ag nanocrystals in $AgNO_3$/PVP composite nanofibers exposed to the UV lamp.

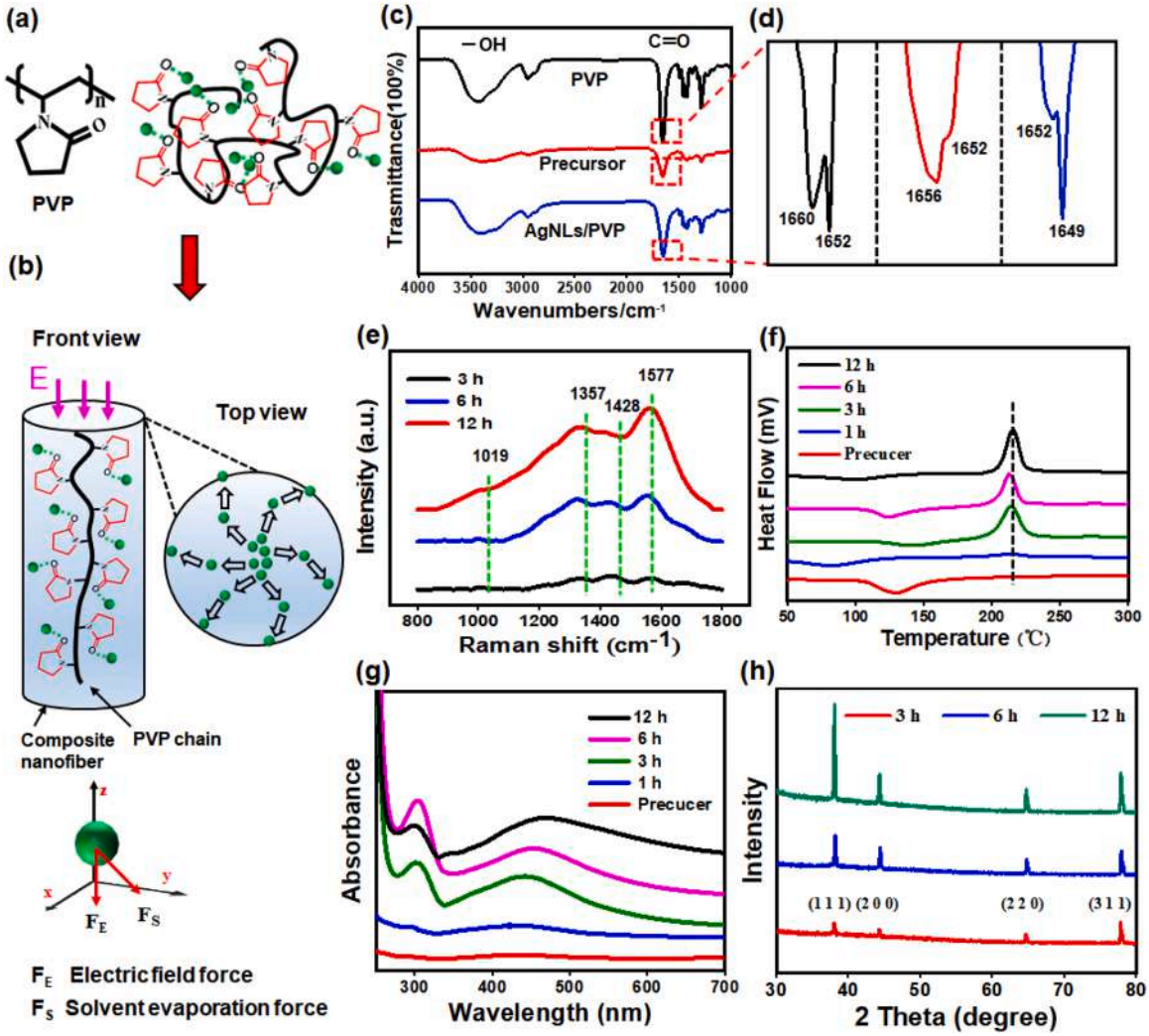

Fig. 2. Migrated and molecular mechanism of the composite nanofibers in the electrospun process and UV irradiation. (a), The attachment of Ag^+ in the complexing groups of PVP molecules. (b), The views of stretched PVP chains and the moved paths of Ag^+ by the electric field force (F_E) and solvent evaporation force (F_S) in the electrospinning. (c), FTIR spectra of the prepared PVP, $AgNO_3$/PVP precursor and AgNLs/PVP nanofibers. (d), The enlarged spectra of C═O peaks around 1660 cm^{-1}. (e), Raman spectra of the AgNLs/PVP nanofibers after 3, 6 and 12 h of UV irradiation. (f,g), DSC results (f) and UV-Vis spectra (g) of the precursor and AgNLs/PVP nanofibers after 1, 3, 6 and 12 h of UV irradiation. (h), XRD results of AgNLs/PVP nanofibers during UV irradiation.

1577 cm^{-1} increase with the passage of irradiation time, suggesting the existence of the amorphous carbon produced by PVP degradation. Moreover, the disappeared characteristic of the peak attributed to C−C bond around 1428 cm^{-1} after 12 h of UV irradiation also confirms the degradation of PVP (Fig. S4).

The directed structure of AgNPs on PVP surface was further produced by the reduction of Ag^+ and the degradation of PVP under UV irradiation. From the scanning electron microscopy (SEM) images of the samples with different irradiation time (Fig. S5), we found that the disappearing morphology of the nanofibers was more obvious when the reaction time was further extended. After 6 h of UV irradiation, no nanofiber profile existed and Ag nanoparticles were mostly distributed in the boundary of the nanofibers, then well-organized pair AgNLs were aligned in the elongating direction of PVP nanofibers at 12 h. The results of differential scanning calorimetry (DSC) are shown in Fig. 2 f, the increasing intensity of adsorption peak around 220° indicates that the growth of Ag nanocrystals and the molecule crosslinking hinder the decomposition of PVP. UV–vis spectra also verify the degradation process of PVP and the growth of Ag nanocrystals (Fig. 2 g). The adsorption peak at 295 nm belongs to the free radicals after PVP degradation, and increases before irradiation for 6 h but decreases at 12 h of the irradiation, further indicating that the free radicals mostly crosslink when Ag^+ are totally reduced. The X-ray diffraction (XRD) spectra reveal the formation of AgNLs at the expense of AgNPs fusion, and confirm that the AgNPs are pure Ag crystals without other silver oxidation after 3 h of UV irradiation (Fig. 2 h).

We further demonstrated the key mechanism of PVP nanofibers as the molecule-directed template for the formation of pair aligned AgNLs as shown in Fig. 3a. Ag ions attaching along the PVP chains in the composite nanofibers are reduced to Ag^0 because of the wild reducibility of PVP and the emitted energy of ultraviolet light. At the beginning of UV irradiation, some Ag nucleus formed and then grew to small single-particle (equation I), giving the credit to Ostwald ripening growth dynamics. Simultaneously, photo-degradation (equation II) and photo-crosslinking (equation III) promoting the reduction of Ag^+ occurred in the irradiated PVP nanofibers. As the reaction proceeds, Ag single-particles in the nanofibers fused together and moved sideways due to the induced energy of free radicals in the broken PVP chains, forming the pair nanostructure of single-particle assembled Ag at the boundary of the original nanofiber locations. So far, expectantly, the multi-stage template technology could be an effective strategy for assembling single-nanoparticle Ag into the pairwise and directed AgNLs.

To gain further insight into the directed nanostructure of AgNLs, we prepared the parallel pattern of the electrospun $AgNO_3$/PVP precursor

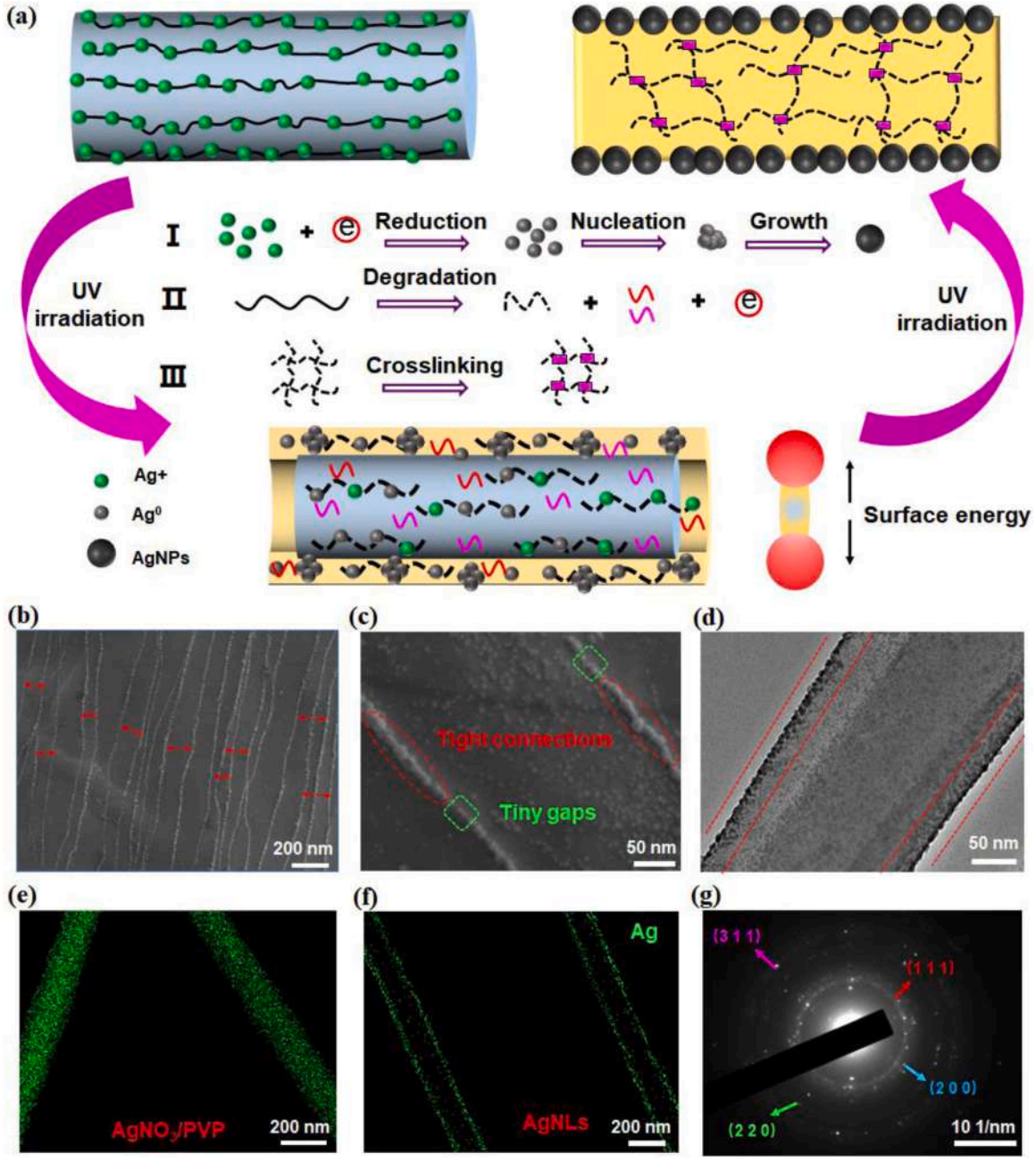

Fig. 3. Assembly mechanism and geometric nanostructure of AgNLs. (a), The single-particle assembly of AgNLs in UV irradiation process, including the Ag^+ reduction (I), PVP degradation (II) and PVP crosslinking (III). (b), SEM image of pair directed AgNLs. (c), Enlarged SEM image of the Ag nanocrystals with tight connections and a few gaps in AgNLs. (d), TEM image of the assembling Ag nanocrystals distributed along the boundary of the composite nanofiber. (e,f), EDS image of the Ag element mapping in $AgNO_3$/PVP nanofibers (e) and AgNLs/PVP nanofibers (f). (g), SAED of the Ag nanocrystals in AgNLs.

nanofibers. Fig. 3b presents SEM image of the AgNLs after 12 h of UV irradiation, the approximately paralleled AgNLs are observed along the extension direction of the nanofiber edges. Fig. 3c,d show the geometric nanostructure of AgNLs with single-particle assembly on the initial nanofiber sites, which is further confirmed by the change in the location distribution of Ag element mapping between $AgNO_3$/PVP precursor nanofibers (Fig. 3e) and AgNLs (Fig. 3 f). Clear lattice fringes corresponding to the interplanar spacing d = 0.234 nm (Fig. S6) and the selected area electron diffraction (SAED) image (Fig. 3 g) display the characteristic of Ag nanocrystals. Moreover, more obvious evidence of two Ag nanocrystals with tight connection (Fig. S6a) and an interval (Fig. S6b) could be spotted in detail. Other elements distributed in $AgNO_3$/PVP nanofibers (Fig. S7) have no transfer effect in AgNLs via 12 h of UV irradiation (Figs. S8 and S9).

The performance of the fabricated AgNLs is depended on the nanoscale arrangement of Ag crystals. By controlling the deposition of PVP templates in electrospinning process, we can get the arbitrary AgNLs patterns such as spiral array, uniaxial parallel array and biaxial crossed array (Fig. S10). The electrochemical performances of the as-prepared AgNLs with different arrays were evaluated in coin cell using the Nyquist plot at the frequency range from 1 to 100 KHz. Fig. 4a-c shows the impedance curves of three patterned AgNLs. The interfacial properties and the impedance data are fitted with an equivalent circuit (Fig. S11), where the interfacial capacitance (C_{dl}) is in parallel with the diffusion impedance (W) and the charge transfer resistance (Rct). Clearly, the ionic conductivity of the formed AgNLs increases with UV

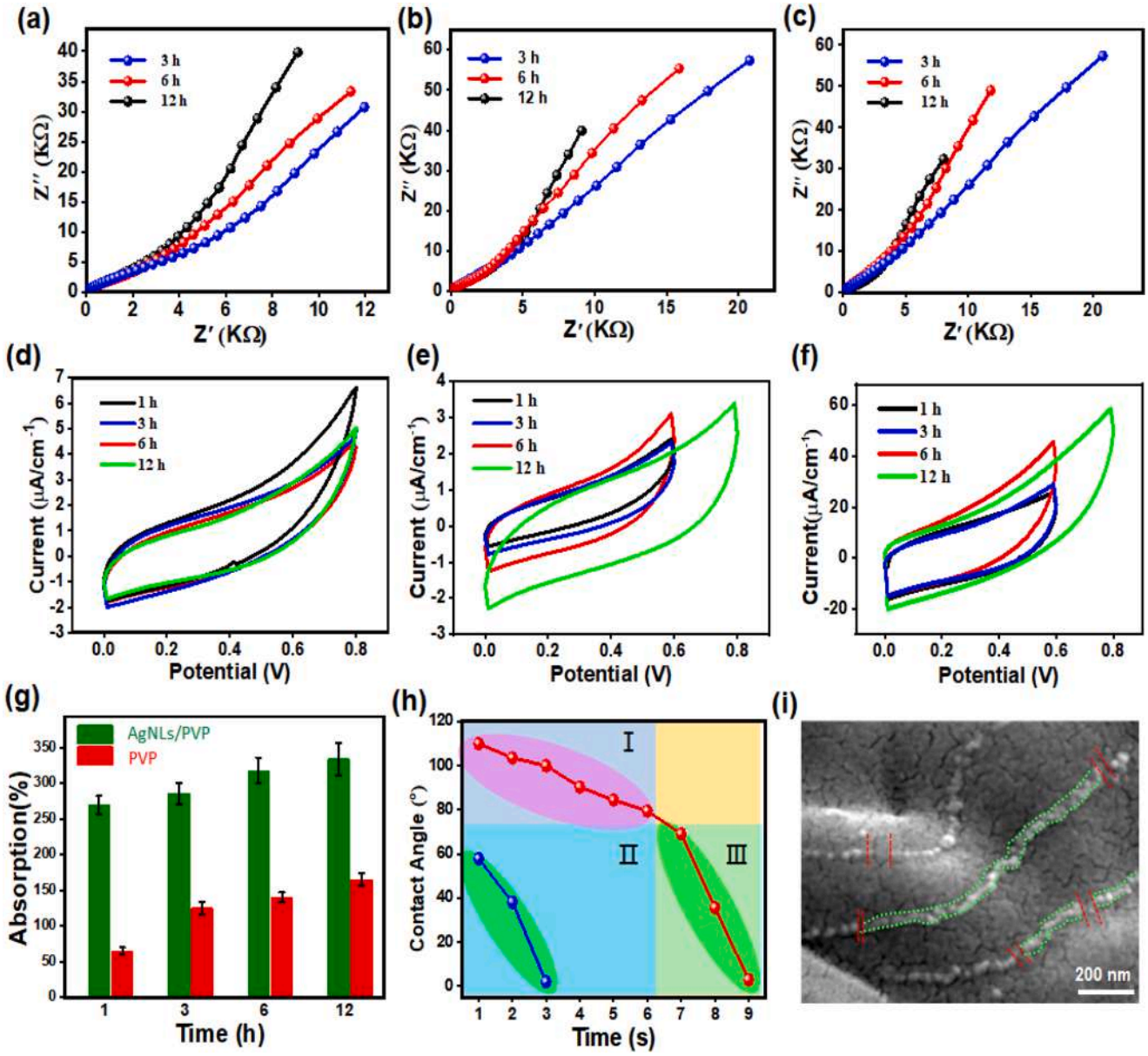

Fig. 4. Electron transport properties of AgNLs with the adsorption of water molecules. (a-c), Impedance of AgNLs with the patterns of spiral array (a), uniaxial parallel array (b) and biaxial crossed array (c) after 3, 6 and 12 h of UV irradiation. (d-f), Cyclic voltammogram curves of AgNLs with three patterns of spiral array (d), uniaxial parallel array (e) and biaxial crossed array (f) during UV irradiation. (g), Water adsorption of AgNLs/PVP composite nanofibers and pure PVP nanofibers. (h), The relationship of the relative contact angle and time for AgNLs/PVP composite nanofibers and pure PVP nanofibers. (i), SEM image of AgNLs/PVP composite nanofibers after absorbing water.

irradiation time. Interestingly, compared with other patterns, AgNLs with the uniaxial parallel pattern exhibit higher ability of ionic conductivity and a weak capacitance behavior at lower frequency region.

We further detected the cyclic voltammograms of the different patterned AgNLs (Fig. 4d-f). Obviously, the cyclic curves show the certain capacitance performance of AgNLs, though the corresponding currents are small. The comparison results of three types of AgNLs on the charge capacity are roughly the same as the differences on electrochemical impedance spectroscopy (EIS), AgNLs with uniaxial parallel arrays show the most outstanding capacitance performance because of the ordered charge transfer in the directed AgNLs.

To explore the water-tolerant properties and the interfacial behavior between AgNLs and H_2O molecules, we investigated the water absorption rate and water contact angle of AgNLs/PVP nanofiber films compared with pure PVP nanofiber film under UV irradiation. It is evident that the water absorption rates of all films are gradually increased with increase of the irradiation time (Fig. 4 g). Moreover, the water absorption rate of AgNLs/PVP films reaches up to 330% while pure PVP film just has 150%. In addition, Fig. S12 shows the different water contact angels of AgNLs/PVP and PVP films, suggesting the sustainable capacity of water adsorption of the composite film with pair directed AgNLs. By comparing the two curves in Fig. 4 h, we find that the gradient trend and range of the red curve from 7 to 9 S (region III) are similar to that of the blue curve (region II), which demonstrates the same adsorption process of H_2O molecules through the PVP networks. However, the slow gradient of the red curve in the first 6 S (region I) is due to the specific adsorption of AgNLs in the AgNLs/PVP film. Fig. 4i shows the SEM image of AgNLs/PVP film after absorbing H_2O molecules, the close connected and slight gaped nanostructure in each nanoline and between the pair nano-lines may precisely lead to the special conductivity when the different amounts of water exist.

We designed a nanoscale AgNLs based humidity sensor (ABHS) that

the AgNLs perpendicularly deposited to the gold interdigital electrode as the sensing material on the polyethylene terephthalate (PET) as the substrate (Fig. 5a). Fig. 5b and c show the digital photos of the ABHS and its bend state. For the humidity sensor, electron transfer is the dominating effect for this liquid–solid electrification process of the polymeric surface [43,44], thus, the orderly assembled AgNLs with a few gaps easily form the conductive path after H_2O molecules fill the gaps, exhibiting high sensitivity for the tiny humidity changes in the environment. The water sensitivity at the different humidity includes the following three stages. First, when the ABHS is exposed to the low RH, few H_2O molecules prefer to fill in the gaps of the contiguous Ag nanoparticles in the AgNLs, and rapidly form the unidirectional conductive paths between the interdigital electrodes (Fig. 5d). In the second stage, with RH increases, some H_2O molecules adsorb on the

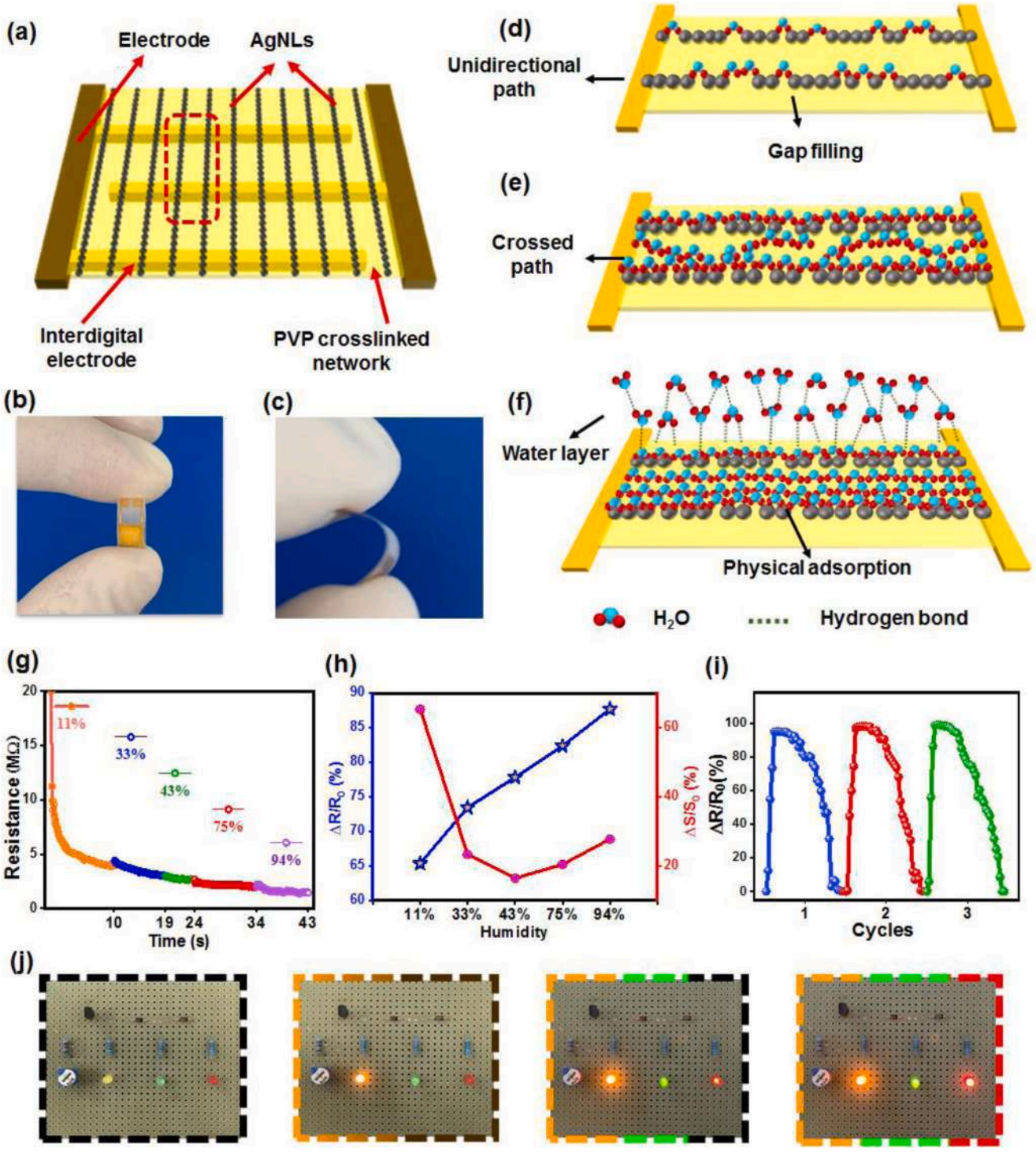

Fig. 5. Sensing mechanism and application of ABHS in ambient humidity monitoring. (a), The interdigital electrode composed of APHS. (b-c), The digital photos the front (b) and side (c) of the fabricated ABHS interdigital electrode. (d-f), The adsorption mechanism of H_2O molecules in ABHS at low (d), middle (e) and high (f) RH. (g), Real-time resistance response of ABHS from 11% to 94% RH. (h), The change in $\Delta R/R_0$ and $\Delta S/S_0$ of ABHS from 11% to 94% RH. (i), The cyclic performance of the real-time resistance response of the ABHS between the ambient 0% and 94% RH. (j), The real-time digital photos of the humidity monitoring of ABHS using the LED lights with three colors from 0% to 94% RH. Yellow light on at 11%, green light on at 43% and red light on at 75% RH.

surface of Ag nanoparticles between the AgNLs array, and form the crossed conductive channel (Fig. 5e). Finally, more H_2O molecules will be absorbed by the degraded PVP network at a high RH, and form the physical adsorption of water layers until reach the saturation (Fig. 5 f).

To illuminate the non-contact response mechanism of H_2O molecules adsorbed on the ABHS, we tested the dynamic resistance response in five humidity conditions (RH values of 11%, 33%, 43%, 75% and 94%) simulated by the saturated salt solutions (Fig. S13). Meanwhile, the environment humidity was always kept at a constant value. As shown in Fig. 5 g, the real-time resistance significantly decreases with the increase of RH value, exhibiting excellent humidity sensing performance. However, Fig. S14 shows the contrary tendency of the real-time resistance response due to the reversibility of ABHS in the desorption process of H_2O molecules. Moreover, we found that the response curves were not linear and the real-time resistance dropped in the initial stage rapidly, this was different from the traditional humidity sensors with linearly varying feature [45,46].

Therefore, we further analyzed the humidity sensitivity of ABHS by carrying out a fitting according to the response curves of the real-time resistance. The resistance response curve from 0% to 11% RH could be fitted into a two-factor exponential equation (Fig. S15), where the parameter A_1 and A_2 respectively correspond to the response degree of the filling in the gaps and the connecting between AgNLs by H_2O molecules. The exponential relationship allows the quick response and high sensitivity at low RH benefiting from the formation of conductive pathways in the initial water sensitivity stage. Interestingly, the resistance of ABHS changes from 11% to 75% RH slowly, which is fitted to a binomial function equation (Fig. S16), demonstrating that there are also two influence factors in this response process. In general, the fitted results prove the nanoscale sensitivity mechanism that the adsorption of water on the surface of AgNLs and PVP could not cause much electron transfer, whereas, the electron transfer speed from one H_2O molecule to another connecting in the AgNLs is faster. Similarly, a single exponential function equation fitted by the response curve from 75% to 94% RH also confirms the mechanism (Fig. S17). The slight fluctuation of the resistance response may be described to the fact that the swelling of PVP crosslinked network at high RH leads to the incidental disconnection of Ag nanoparticles in AgNLs.

We quantitatively investigated the change degree of the real-time resistance compared to the initial resistance for the ABHS (Fig. 5 h). The trend of $\Delta S/S_0$ values (where $S = \Delta R/R_0$, R and R_0 are the real-time and initial resistance, S and S_0 are real-time and last $\Delta R/R_0$) confirms the different degree of the resistance response in above-mentioned three stages of the humidity sensitivity. Fig. 5i shows the typical real-time resistance response of ABHS between the ambient 0% and 94% RH, suggesting the excellent dynamic stability. Moreover, the ABHS exhibits the fast response time (< 0.9 S) and recovery time (< 3.1 S) when RH increases from 45% to 75%, as shown in Fig. S18. The response and recovery speed are the key factors of sensing performance. We further found that the ABHS had the different response and electrodynamic behaviors at low and high RH.

Importantly, the ABHS has the fast response speed at low RH especially, so that, it can result in the greater potential of nanoscale application in humidity monitoring, non-contact control and respiratory monitoring. Thus, we developed an ambient humidity monitoring system, including a recording multimeter of real-time resistance and a circuit bord with the ABHS (Fig. S19), and used three LED lights with yellow, green and red colors to imply the different degrees of the ambient humidity. The monitoring circuit diagram was interestingly simulated by PROTEUS software to calculate the range of the resistance when the different light was on (Fig. S20).

Fig. 5j displays the real-time digital photos of the monitoring device at three RH. As seen in Movie S1, based on the accurate design of the threshold value according to the real-time resistance, when the ambient humidity is below 11%, no LED is lighted. But when RH reach to 33%, 43% and 75% in turn, the yellow, green and red LED lights are turned on successively. Herein, theoretically, as long as the resistance value corresponding to a certain RH for the ABHS is calculated, we can accurately detect the ambient RH from 0% to 100% in any environment.

Supplementary material related to this article can be found online at doi:10.1016/j.nanoen.2021.106748.

The excellent response capability of AgNLs at low humidity makes the ABHS possible to be applied in nanoscale non-contact device such as the sensitive electro-tactile system on the skin of the finger [47]. Fig. 6a shows the schematic diagram of the non-contact switch based on the fingertip humidity. When the fingertip approaches to the sensor, the water molecules from the fingertip will diffuse on the sensor, and then, the resistance value decreases rapidly because of the connection of electron-transfer path in AgNLs. Inversely, the resistance value increases when the fingertip rapidly removes away the sensor.

Thus, we fabricated the non-contact flexible sensor consisting of the ABHS embedded on the surface of the transparent epoxy resin and the wires through the resin (Fig. S21). The advantage of the sensor is that the preparation process is simple and the use is widespread as the flexible device such as the fingerprint lock and the non-contact visual gesture control. Movie S2 shows the real-time response of the sensor during the fingertip approaches to the sensor till 5 mm and rapidly moves away from the sensor after staying 2 S. The blue and red curves respectively represent the fingertip at normal and sweaty state (more water on the surface of the fingertip). As the result shown in Fig. 6b, when the fingertip approaches the sensor, the resistances at two states decrease rapidly, but it has smaller threshold valve and longer recovery time at sweaty state than at normal state.

Supplementary material related to this article can be found online at doi:10.1016/j.nanoen.2021.106748.

Given the sensitivity of the device, we can set the threshold valve and recovery time range of the resistance to remind users. We further demonstrated the reproducibility and stability of the fingertip sensor at two states by the test of 10 cycles (Fig. 6c). Moreover, the use of long time for the sensor by recording the results twice a day during 20 consecutive days also verified the durability of the ABHS as a non-contact humidity device (Fig. S22).

In addition, we found that the ABHS had great potential in respiratory monitoring by detecting the subtle change of water. As shown in Fig. 6d, when the gas exhaled from our nose passes through the ABHS, the carried water vapor molecules are quickly captured and adsorbed by the hydrophilic PVP network, leading to the change in inherent electrical conductivity of the directed AgNLs. Therefore, the health states with the different respiration rates could be determined by the waveform and amplitude of the monitoring curves. Fig. 6e shows the various responses of ABHS, the gas exhalations in “healthy”, “weak”, “kinetic” and “ailing” conditions correspond to the respiratory rates of 20, 25, 35 and 15 times/min. We found that the breathing signals in four respiratory conditions were smooth but had the respective waveform and amplitude. Obviously, the amplitude increased as the respiratory rate decreased, because the faster breathing would prevent the response signal from restoring to the initial level and promptly response to the next adsorption of H_2O molecules.

Next, the data of the resistance response in one minute were analyzed using the digital boxplots (Fig. 6 f). We could quantificationally estimate the respiratory rate from the median value of the resistance, the slower breathing enabled the resistance signal of ABHS to result in a high level. The prolonged real-time monitoring of breathing was very effective for the patients with respiratory diseases such as sleep apnea syndrome. Here, we recorded the response signal of breathing when the testing object just slept and fell asleep with 30 min (Fig. 6 g). The fairly smooth signals were obtained in both breathing stages, moreover, the slight fluctuation from the continuous but uneven breathing curve was also detected.

Thus, as long as the breathing of the testing object is normally, the detected signal will keep steadily. Whereas, if the signal decreases significantly and exceeds the threshold value, indicating that the testing

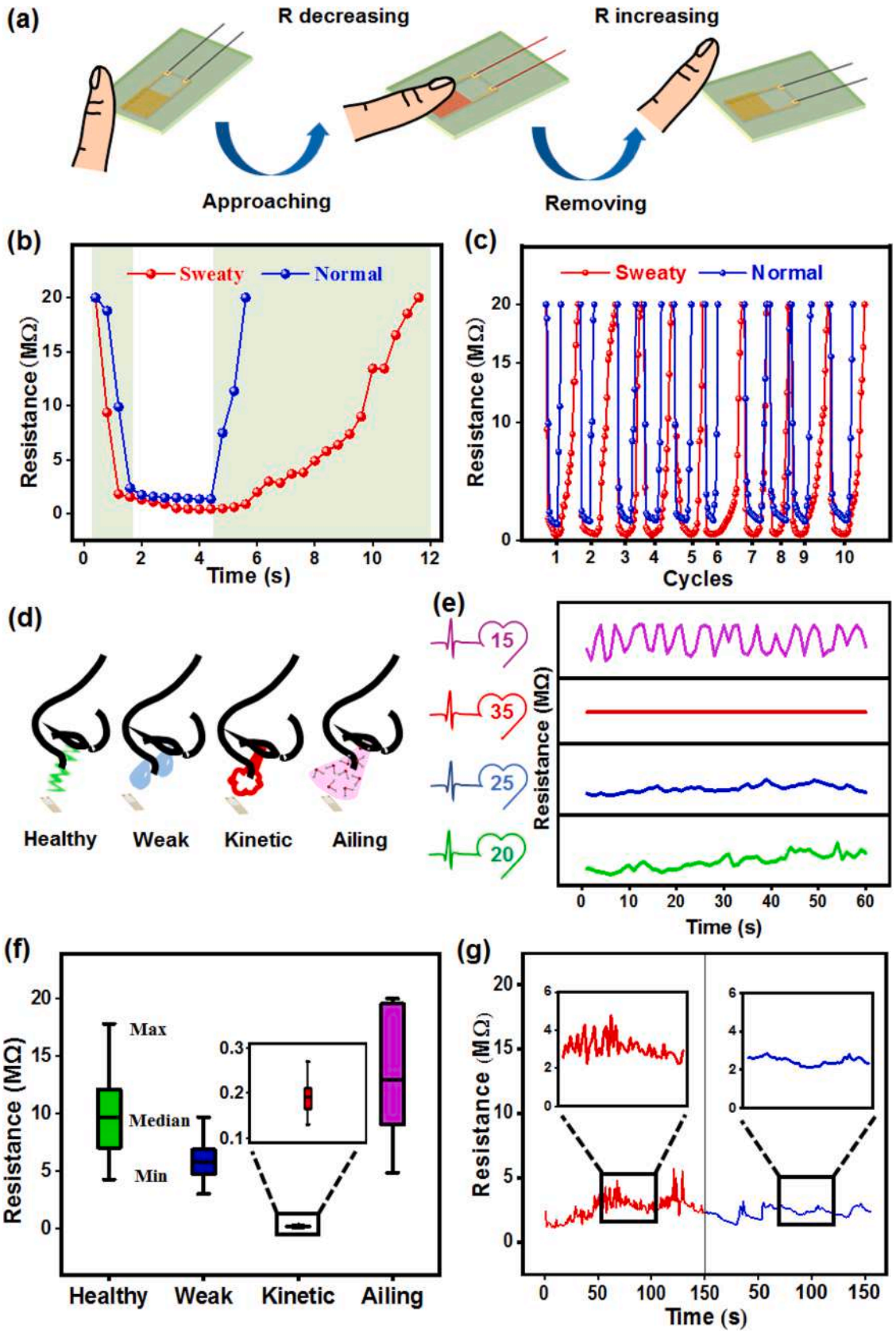

Fig. 6. Application of ABHS in non-contact switch and respiratory monitoring. (a), Resistance response of ABHS as non-contact switch. (b), Real-time resistance of ABHS when the fingertips with sweaty and normal states close to it. (c), The test of 10 cycles of the fingertip sensor at sweaty and normal states. (d), The representative monitoring in "healthy", "weak", "kinetic" and "ailing" respiratory conditions. (e), Effect of the respiratory rates at the rate of 20, 25, 35 and 15 times per minutes on relative resistance of ABHS. (f), Box plots of the monitoring curves for ABHS at the four respiratory conditions. (g), Record of the resistance response of ABHS with the respiration data of 150 s when the testing object just slept and 30 min after falling asleep.

object changes the breathing and has been an unexpected attack, the device can send out warring signals by the rapid result analysis of the subtler breathing change.

3. Conclusion

In summary, we have developed a new synthesis method combining the electrospinning and in-situ UV irradiation at room temperature to fabricate the pair directed AgNLs arrays. Using the complexed and field-transferred template effect of PVP chains, the Ag+ /PVP complex was uniformly dispersed in the composite precursor, and then diffused from the inside of the polymeric chains to the nanofiber boundary in the electrospun process. Further, Ag nanocrystals assembled to the single-particle connected lines along the both sides of the composite nanofibers by the degradation and crosslinking of PVP chains under UV irradiation. Compared with the conventional linear responded humidity sensor, the fabricated ABHS exhibited excellent sensitivity at low RH and special response due to the nano-structured gaps in the contiguous AgNLs. The further explorations of the humidity monitoring device, non-contact switch of fingertip and real-time respiratory monitoring demonstrated the feasibility and stability of the ABHS as a nanoscale device. Given the conductive mechanism of AgNLs arrays at low, middle and high humidity, the non-contact ABHS would provide an avenue for the consumer health and biomedical sensors.

4. Experimental Section

4.1. Synthesis of $AgNO_3$/PVP nanofibers

The precursor solution was prepared using the following procedure. First, 1.32 g PVP were dissolved in 10 ml mixture of deionized water and ethyl alcohol (H_2O:CH_2OH=3:2) and magnetically stirring for 4 h until completely dissolved at room temperature. Next, 0.013 (1 wt%), 0.051 (3 wt%), 0.066 (5 wt%) and 0.105 g (8 wt%) $AgNO_3$ were added into the solution and stirring for 24 h to mix the uniformly forming electrospinning solution. Using a 5 ml syringe to aspirate the spinning solution, removed air bubbles in the spinning solution, connected to the stainless steels spinning nozzle (inner diameter is 0.7 mm), and then fixed the syringe horizontally on the microfluidic injection pump, clean and grounded aluminum foil received the nanofibers. The aluminum foil was 10 cm away from the nozzle, the voltage was 15–20 kV, and the micro-flow pump speed was 0.2–0.5 ml/h. The electrospinning process was completed at room temperature.

4.2. Preparation of Ag nano-lines (AgNLs)

To reduce the Ag^+ into Ag^0 forming AgNLs, the $AgNO_3$/PVP nanofiber films were located under the UV lamp (200 W, 365 nm) with distance of 10 cm. In order to ensure the $AgNO_3$/PVP nanofiber films were irradiated uniformly, we put the films perpendicular to the direction of the lamp source. The AgNLs were obtained after the continuous UV irradiation.

4.3. Fabrication of AgNLs based humidity sensor (ABHS)

We used an interdigital electrode as the collector in electrospinning process for 30 min, in which the $AgNO_3$ concentration was 5 wt%, and then irradiated by UV lamp for 12 h to obtain ABHS. Finally, the samples were placed into a vacuum drying oven to remove the small molecules and achieve the long-term storage.

4.4. Water absorption capability test

The as-prepared AgNLs/PVP films and pure PVP film were uncovered from the aluminum foil and cut into a square (1 ×1 cm). Then recorded the weight of the films in the dry state (M_1) and after dipped in the deionized water for 24 h (M_2). The water absorption rate was calculated from the following equation.

$$\text{Absorption} = \frac{M_1}{M_2} \times 100\%$$

4.5. Resistance response test of ABHS

Two conductive wires were connected at both ends of the electrode of ABHS for resistance test using a digital multimeter (Victor VC890C$^+$). The ABHS was placed directly above the liquid level of the solution with the presetting humidity and recorded the resistance values until the test value was stable, then quickly put into next different humidity environment to obtain the real-time resistance response curves. During the test process in lab, the environment humidity was always kept at 40% by a dehumidifier.

4.6. Fabrication and resistance response test of ABHS as the ambient humidity monitoring system

To fabricate the humidity monitoring system, we designed an amplifying circuit (Fig. S19) with three LED lights to show the changed resistances. All components were welded on a circuit board according to the schematic circuit. Then the ABHS was placed in different ambient humidity with the power on and recorded the current response of ABHS (Video S1).

4.7. Characterization

The morphologies of the AgNLs were investigated by field-emission scanning electron microscopy (FE-SEM, JSM-7800 F, JEOL, Japan). The morphologies of the AgNLs were observed by a field-emission transmission election microscope (FE-TEM, JEM-2100 F, JEOL, Japan) operating at 200 KV. Fourier transform infrared spectroscopy (FT-IR) spectra of all samples were carried out using a Nicolet 5700 spectrometer. Raman spectra (Raman) spectra of all samples were obtained using a Lab Spec 6 spectrometer with a 532 nm blue laser beam. The as-prepared films were directly tested after drying. Differential scanning calorimetry (DSC) Q100 modulated differential scanning calorimeter of TA Instruments was used to analyze the thermal behavior of the samples in N_2 atmosphere. UV adsorption spectra (UV-Vis) were taken from the dissolved AgNLs in water by ultraviolet spectrophotometer (UV–vis, UV-2550, Shimadu). X-ray diffractometry (XRD, Philips, X′Pert PRO, Netherlands) was used to determine the crystallization property of the AgNLs. Water contact angle (WCA) of the as-prepared films were assessed using the sessile drop method at room temperature by a video contact angle instrument (DSA 100, Kruss, Germany).

CRediT authorship contribution statement

Jing He: Conceptualization, Visualization, Methodology, Formal analysis, Writing-original draft. **Xiaotong Zheng:** Writing-review & editing, Funding acquisition, Supervision. **Zhiwen Zheng:** Conceptualization, Methodology, Visualization. **Degang Kong:** Conceptualization, Visualization, Methodology. **Kai Ding:** Visualization, Methodology, Investigation. **Ningjun Chen:** Investigation. **Haitao Zhang:** Investigation. **Weiqing Yang:** Funding acquisition, Supervision.

Declaration of Competing Interest

The authors declare that they have no known competing financial interests or personal relationships that could have appeared to influence the work reported in this paper.

Acknowledgments

X.Z. is funded by Sichuan Science and Technology Program, China (No. 2021YFH0129), the Fundamental Research Funds for the Central Universities, China (No. 2682021ZTPY062). The authors acknowledge Youth Science and Technology Innovation Research Team Funds of Sichuan Province, China (No. 20CXTD0106 and NO. 2016TD0026).

Appendix A. Supporting information

Supplementary data associated with this article can be found in the online version at doi:10.1016/j.nanoen.2021.106748.

References

[1] T. Yang, H. Yang, S.J. Zhen, C.Z. Huang, Hydrogen-bond-mediated in situ fabrication of AgNPs/Agar/PAN electrospun nanofibers as reproducible SERS substrates, ACS Appl. Mater. Interfaces 7 (2015) 1586–1594.
[2] A.M. Elseman, W. Sharmoukh, S. Sajid, P. Cui, J. Ji, S. Dou, D. Wei, H. Huang, W. Xi, L. Chu, Y. Li, B. Jiang, M. Li, Superior stability and efficiency over 20% perovskite solar cells achieved by a novel molecularly engineered Rutin–AgNPs/thiophene copolymer, Adv. Sci. 5 (2018), 1800568.
[3] L. Zhang, Q. Cheng, C. Li, X. Zeng, X.-Z. Zhang, Near infrared light-triggered metal ion and photodynamic therapy based on AgNPs/porphyrinic MOFs for tumors and pathogens elimination, Biomaterials 248 (2020), 120029.
[4] C. Zhang, S. Govindaraju, K. Giribabu, Y.S. Huh, K. Yun, AgNWs-PANI nanocomposite based electrochemical sensor for detection of 4-nitrophenol, Sens. Actuators, B 252 (2017) 616–623.
[5] Z. Ma, S. Kang, J. Ma, L. Shao, Z. Ji, High-performance and rapid-response electrical heaters based on ultraflexible, heat-resistant, and mechanically strong aramid nanofiber/Ag nanowire nanocomposite papers, ACS Nano 13 (2019) 7578–7590.
[6] P. Tang, X. Zheng, H. Yang, J. He, Z. Zheng, W. Yang, S. Zhou, Intrinsically stretchable and shape memory conducting nanofiber for programmable flexible electronic films, ACS Appl. Mater. Interfaces 11 (2019) 48202–48211.
[7] S. Lin, X. Bai, H. Wang, H. Wang, J. Song, K. Huang, C. Wang, N. Wang, B. Li, M. Lei, H. Wu, Roll−to−roll production of transparent silver−nanofiber−network electrodes for flexible electrochromic smart windows, Adv. Mater. 29 (2017), 1703238.
[8] Y. Zhang, Z. Huo, X. Wang, X. Han, Z.L. Wang, High precision epidermal radio frequency antenna via nanofiber network for wireless stretchable multifunction electronics, Nat. Commun. 11 (2020) 5629.
[9] X. Qin, D. Luo, Z. Xue, Q. Song, T. Wang, Self−assembled Ag−MXA superclusters with structure−dependent mechanical properties, Adv. Mater. 30 (2018), 1706327.
[10] X.Y. Zhang, A. Hu, T. Zhang, L. Wei, W.W. Duley, Self-assembly of large-scale and ultrathin silver nanoplate films with tunable plasmon resonance properties, ACS Nano 5 (2011) 9082–9092.
[11] N. Li, D. Pranantyo, E.-T. Kang, D.S. Wright, H.-K. Luo, A simple drop-and-dry approach to grass-like multifunctional nanocoating on flexible cotton fabrics using in situ-generated coating solution comprising titanium-oxo clusters and silver nanoparticles, ACS Appl. Mater. Interfaces 12 (2020) 12093–12100.
[12] Z. Zeng, F. Jiang, Y. Yue, D. Han, J. Wang, Flexible and ultrathin waterproof cellular membranes based on high−conjunction metal−wrapped polymer nanofibers for electromagnetic interference shielding, Adv. Mater. 32 (2020), 1908496.
[13] F. Ershad, A. Thukral, J. Yue, P. Comeaux, C. Yu, Ultra-conformal drawn-on-skin electronics for multifunctional motion artifact-free sensing and point-of-care treatment, Nat. Commun. 11 (2020) 3823.
[14] M. Yang, J. Yu, F. Lei, H. Zhou, Y. Wei, B. Man, C. Zhang, C. Li, J. Ren, X. Yuan, Synthesis of low-cost 3D-porous ZnO/Ag SERS-active substrate with ultrasensitive and repeatable detectability, Sens. Actuators, B 256 (2018) 268–275.
[15] Y. Li, P. Zhang, Z. Ouyang, M. Zhang, Z. Lin, J. Li, Z. Su, G. Wei, Nanoscale graphene doped with highly dispersed silver nanoparticles: quick synthesis, facile fabrication of 3D membrane-modified electrode, and super performance for electrochemical sensing, Adv. Funct. Mater. 26 (2016) 2122–2134.
[16] C. Shi, J. Wang, M.L. Sushko, W. Qiu, X.Y. Liu, Silk flexible electronics: from Bombyx mori silk Ag nanoclusters hybrid materials to mesoscopic memristors and synaptic emulators, Adv. Funct. Mater. 29 (2019), 1904777.
[17] S. Lin, H. Wang, F. Wu, Q. Wang, X. Bai, D. Zu, J. Song, D. Wang, Z. Liu, Z. Li, Room-temperature production of silver-nanofiber film for large-area, transparent and flexible surface electromagnetic interference shielding, npj Flex. Electron 3 (2019) 6.
[18] L. Wang, H. Qiu, C. Liang, P. Song, Y. Han, Y. Han, J. Gu, J. Kong, D. Pan, Z. Guo, Electromagnetic interference shielding MWCNT-Fe3O4@Ag/epoxy nanocomposites with satisfactory thermal conductivity and high thermal stability, Carbon 141 (2019) 506–514.
[19] H. Wang, C. Ji, C. Zhang, Y. Zhang, Z. Zhang, Z. Lu, J. Tan, L.J. Guo, Highly transparent and broadband electromagnetic interference shielding based on ultrathin doped Ag and conducting oxides hybrid film structures, ACS Appl. Mater. Interfaces 11 (2019) 11782–11791.
[20] C. Yang, Y. Yao, S. He, H. Xie, E. Hitz, L. Hu, Ultrafine silver nanoparticles for seeded lithium deposition toward stable lithium metal anode, Adv. Mater. 29 (2017), 1702714.
[21] A. GhavamiNejad, A.R. Unnithan, A.R.K. Sasikala, M. Samarikhalaj, R.G. Thomas, Y.Y. Jeong, S. Nasseri, P. Murugesan, D. Wu, C.H. Park, C.S. Kim, Mussel-inspired electrospun nanofibers functionalized with size-controlled silver nanoparticles for wound dressing application, ACS Appl. Mater. Interfaces 7 (2015) 12176–12183.
[22] D. Gan, W. Xing, L. Jiang, J. Fang, C. Zhao, F. Ren, L. Fang, K. Wang, X. Lu, Plant-inspired adhesive and tough hydrogel based on Ag-Lignin nanoparticles-triggered dynamic redox catechol chemistry, Nat. Commun. 10 (2019) 1487.
[23] A.-C. Burduşel, O. Gherasim, A.M. Grumezescu, L. Mogoantă, A. Ficai, E. Andronescu, , Biomedical applications of silver nanoparticles: An up-to-date overview, Nanomaterials 8 (2018) 681.
[24] X. Xia, J. Zeng, L.K. Oetjen, Q. Li, Y. Xia, Quantitative analysis of the role played by poly (vinylpyrrolidone) in seed-mediated growth of Ag nanocrystals, J. Am. Chem. Soc. 134 (2012) 1793–1801.
[25] X. Qi, T. Balankura, Y. Zhou, K.A. Fichthorn, How structure-directing agents control nanocrystal shape: polyvinylpyrrolidone-mediated growth of Ag nanocubes, Nano Lett. 15 (2015) 7711–7717.
[26] Y. Chen, D. Tang, Z. Huang, X. Liu, X. Tang, Stable single atomic silver wires assembling into a circuitry-connectable nanoarray, Nat. Commun. 12 (2021) 1191.
[27] M. Su, F. Li, S. Chen, Z. Huang, M. Qin, W. Li, X. Zhang, Y. Song, Nanoparticle based curve arrays for multirecognition flexible electronics, Adv. Mater. 28 (2016) 1369–1374.
[28] M.-F. Lin, J. Xiong, J. Wang, K. Parida, P.S. Lee, Core-shell nanofiber mats for tactile pressure sensor and nanogenerator applications, Nano Energy 44 (2018) 248–255.
[29] X. Peng, K. Dong, C. Ye, Y. Jiang, Z.L. Wang, A breathable, biodegradable, antibacterial, and self-powered electronic skin based on all-nanofiber triboelectric nanogenerators, Sci. Adv. 6 (2020) eaba9624.
[30] S. Gao, N. Wang, S. Li, D. Li, A multi-wall Sn/SnO2@ carbon hollow nanofiber anode material for high-rate and long-life lithium-ion batteries, Angew. Chem., Int. Ed. 132 (2020) 2486–2493.
[31] S. Choi, S.I. Han, D. Jung, H.J. Hwang, C. Lim, S. Bae, O.K. Park, C.M. Tschabrunn, M. Lee, S.Y. Bae, J.W. Yu, J.H. Ryu, S.-W. Lee, K. Park, P.M. Kang, W.B. Lee, R. Nezafat, T. Hyeon, D.-H. Kim, Highly conductive, stretchable and biocompatible Ag–Au core–sheath nanowire composite for wearable and implantable bioelectronics, Nat. Nanotechnol. 13 (2018) 1048–1056.
[32] G. Dong, X. Xiao, X. Liu, B. Qian, Z. Ma, S. Ye, D. Chen, J. Qiu, Preparation and characterization of Ag nanoparticle-embedded polymer electrospun nanofibers, J. Nanopart. Res. 12 (2010) 1319–1329.
[33] L. Tian, P. Wang, Z. Zhao, J. Ji, Antimicrobial activity of electrospun poly (butylenes succinate) fiber mats containing PVP-capped silver nanoparticles, Appl. Biochem. Biotechnol. 171 (2013) 1890–1899.
[34] L.C. Lopérgolo, A.B. Lugão, L.H. Catalani, Direct UV photocrosslinking of poly (N-vinyl-2-pyrrolidone) (PVP) to produce hydrogels, Polymer 44 (2003) 6217–6222.
[35] S.E.H. Murph, C. Murphy, A. Leach, K. Gall, A possible oriented attachment growth mechanism for silver nanowire formation, Cryst. Growth Des. 15 (2015) 1968–1974.
[36] W. Wang, K. Ouaras, A.L. Rutz, X. Li, M. Gerigk, T.E. Naegele, G.G. Malliaras, Y.Y. S. Huang, Inflight fiber printing toward array and 3D optoelectronic and sensing architectures, Sci. Adv. 6 (2020) eaba0931.
[37] D. Li, Y. Wang, Y. Xia, Electrospinning of polymeric and ceramic nanofibers as uniaxially aligned arrays, Nano Lett. 3 (2003) 1167–1171.
[38] X. Zhang, H. Lin, H. Shang, J. Xu, J. Zhu, W. Huang, Recent advances in functional fiber electronics, SusMat 1 (2021) 105–126.
[39] W. Chao, J.-T. Hsieh, C.-H. Chang, J.J.-M. Lin, Direct kinetic measurement of the reaction of the simplest Criegee intermediate with water vapor, Science 347 (2015) 751–754.
[40] J. Lv, J. Chen, P.S. Lee, Sustainable wearable energy storage devices self-charged by human-body bioenergy, SusMat 1 (2021) 285–302.
[41] O. Karatay, M. Dogan, Modelling of electrospinning process at various electric fields, Micro Nano Lett. 6 (2011) 858–862.
[42] N. Radacsi, F.D. Campos, C.R.I. Chisholm, K.P. Giapis, Spontaneous formation of nanoparticles on electrospun nanofibers, Nat. Commun. 9 (2018) 4740.
[43] S. Li, Y. Fan, H. Chen, J. Nie, Y. Liang, X. Tao, J. Zhang, X. Chen, E. Fu, Z.L. Wang, Manipulating the triboelectric surface charge density of polymers by low-energy helium ion irradiation/implantation, Energy Environ. Sci. 13 (2020) 896–907.
[44] J. Nie, Z. Ren, L. Xu, S. Lin, F. Zhan, X. Chen, Z.L. Wang, Probing contact-electrification-induced electron and ion transfers at a liquid–solid interface, Adv. Mater. 32 (2020), 1905696.
[45] L. Lu, C. Jiang, G. Hu, J. Liu, B. Yang, Flexible noncontact sensing for human–machine interaction, Adv. Mater. 33 (2021), 2100218.
[46] J. Yang, R. Shi, Z. Lou, R. Chai, G. Shen, Flexible smart noncontact control systems with ultrasensitive humidity sensors, Small 15 (2019), 1902801.
[47] Y. Shi, F. Wang, J. Tian, S. Li, E. Fu, J. Nie, R. Lei, Y. Ding, X. Chen, Z.L. Wang, Self-powered electro-tactile system for virtual tactile experiences, Sci. Adv. 7 (2021) eabe2943.

Jing He received her M.D. degree in Biomedical Engineering from Southwest Jiaotong University, P.R. China in 6, 2021. Her major includes biomedical sensors and nano functional materials.

Xiaotong Zheng received his Ph.D degree in Materials Science from Southwest Jiaotong University, P.R. China in 2009. He is now an Associate Prof. in Southwest Jiaotong University. His main reseach interest focus on intelligent biomedical materials, nano sensing materials, nano colloidal motors, and preparation and analysis of bionic micro-nano structures.

Zhiwen Zheng received his B.S. degree in Material Chemistry from Sichuan University, P.R. China in 2019. He is currently pursuing M.D. degree in Biomedical Engineering at Southwest Jiaotong University. His research interest includes preparation and biomedical application of nanomotors based on organic matter.

Degang Kong received his B.S. degree in Material Science and Engineering from Southwest Jiaotong University, P.R. China in 2019. He is currently pursuing M.D. in Material Science and Engineering at SWJTU. His research interest focus on nano electromagnetic materials in biomedicine.

Kai Ding received his B.S. degree in Material Science and Engineering from Southwest Jiaotong University, P.R. China in 2021. He is currently pursuing M.D. degree in mechanical engineering at SWJTU. His research interest includes sensing materials sensors and silver nanoparticles.

Ningjun Chen received her B.S. degree in Material Science and Engineering from Southwest Jiaotong University, P.R. China in 2017. She is currently pursuing Ph.D. degree in materials science and engineering at SWJTU. Her research interest includes two-dimensional materials and energy storage devices.

Haitao Zhang received his Ph.D degree in Electrical Engineering from Institute of Electrical Engineering in 2015, Chinese Academy of Sciences. He is now an Associate Prof. in Southwest Jiaotong University (Chengdu, China). His main reseach interest focus on electrochemical analysis and in-situ technology, electrochemical energy storage devices (supercapacitors and lithium ion batteries) and preparation and characterization of new energy storage materials.

Weiqing Yang received his Ph.D. in Materials Science and Engineering from Sichuan University in 2011. From 2011–2014, he worked as a post-doctorate research fellow in the University of electronic technology and Georgia Institute of technology. Now, he is a Prof. in Southwest Jiaotong University. His main research interest includes multifunctional sensing materials and integrated devices, advanced energy storage materials and devices, and optoelectronic materials and devices.